The angular resolution of the GRAPES-3 array from the shadows of the Moon and the Sun

A. Oshima [a], S.R. Dugad [a], U.D. Goswami [a], S.K. Gupta [a,*], Y. Hayashi [b], N. Ito [b], A. Iyer [a], P. Jagadeesan [a], A. Jain [a], S. Kawakami [b], M. Minamino [b], P.K. Mohanty [a], S.D. Morris [a], P.K. Nayak [a], T. Nonaka [b], S. Ogio [b], B.S. Rao [a], K.C. Ravindran [a], H. Tanaka [a], S.C. Tonwar [a], The GRAPES-3 Collaboration

[a] Tata Institute of Fundamental Research, Mumbai 400 005, India
[b] Graduate School of Science, Osaka City University, Osaka 558-8585, Japan

ABSTRACT

The absence of a well established point source of very high energy ($\gtrsim 10$ TeV) γ-rays in the sky, makes the measurement of the angular resolution and the absolute pointing accuracy of an extensive air shower (EAS) array a challenging task. In the past, several groups have utilized the reduction in the isotropic flux of cosmic rays due to the shadows of the Moon and the Sun, to measure the angular resolution and the absolute pointing accuracy of their arrays. The data collected from the GRAPES-3 EAS array, over the period of 4 years from 2000 to 2003, has been used to observe the shadow of the Moon at a level of $\sim 5\sigma$ and that of the Sun at a lower level of significance. The high density of the detectors in GRAPES-3 enabled an angular resolution of $0.7°$ to be obtained at energies as low as 30 TeV. The angular resolution studies were further extended by using two other techniques, namely, the even–odd and the left–right methods. All three techniques have yielded nearly identical results on the energy dependent angular resolution.

© 2009 Elsevier B.V. All rights reserved.

1. Introduction

The interstellar magnetic fields deflect the charged cosmic rays to travel along complex trajectories within the galaxy resulting in complete loss of information on the location of the cosmic ray sources. This problem could be obviated if one could identify cosmic ray photons which would travel along straight lines, unaffected by the interstellar magnetic field and thereby preserving the directional information of their sources. Therefore, knowledge of the high energy processes that lead to the production and acceleration of cosmic rays to ultra-high energies may be obtained through the study of the cosmic γ-rays.

It is generally agreed that the bulk of the cosmic rays of energies below the 'knee' are produced within our galaxy and are mainly accelerated in supernova explosions, through the diffusive shock acceleration mechanism [1–3]. Therefore, the supernova remnants within the galaxy have been an important target for the observations during the last several decades, over a broad energy region from 100 MeV to beyond a PeV. The discovery of the pulsars in the 1960s and their association with the supernova remnants added to the interest in particle acceleration processes associated with the supernovae. The knowledge that the pulsars are capable of directly accelerating particles to TeV energies and beyond [4–

8] have provided further impetus to these studies. Among the known pulsars and the associated supernova remnants, the CRAB pulsar and its associated nebula have been among the most-studied astronomical objects at all wavelength in the electromagnetic spectrum. The observations of the CRAB pulsar and its associated nebula by the early satellite based instruments such as the SAS-2 and the COS-B, followed by the detailed studies by the EGRET instrument on the Compton Gamma Ray Observatory, established the CRAB as a *standard candle* over the MeV–GeV energy range. These observations also imply the presence of highly relativistic charged particles in the nebula that have been accelerated to energies beyond hundreds of GeV. The discovery of the synchronous pulsed emission from the radio (10^{-5} eV) to GeV γ-rays, emphasized the importance of the pulsar and its role in the acceleration of charged particles in this nebula.

The satellite borne detectors have also provided considerable information on the γ-ray sources and their galactic distribution for energies below 10 GeV. The experimental studies on the sources of photons of energies above 100 GeV require large effective collection area and exposure time, which are presently possible only with the ground based detectors employing the atmospheric Čerenkov technique [9,10]. However, the cosmic sources of ultra-high energy ($\gtrsim 100$ TeV) γ-rays can only be studied using the extensive air shower technique, which permits a sufficiently large area and exposure time factors. Since the γ-ray flux from a source has to be detected, against a huge background con-

tributed by the isotropic flux of the cosmic rays, it is necessary to achieve as good a rejection of this background as possible for the detection system. For a point source, the signal to background ratio is inversely proportional to the square of the angular resolution. Therefore, the most important requirement of an EAS detector system is, its angular resolution for maximizing the signal to background ratio. The technique of relative arrival timing has been used extensively in the EAS arrays, for the determination of the arrival direction of the showers [9,11,12].

The studies of the EAS at energies below 100 TeV involve the detection of the shower electrons that suffer considerable scattering in the atmosphere prior to their detection at the ground level. Therefore, it is expected that the angular resolution attainable with an EAS array would be relatively poorer as compared to an atmospheric Čerenkov detector which involves detection of the Čerenkov photons. Furthermore, the angular resolution of an EAS array is also expected to depend on the shower size 'N_e' at the detection level and it improves with the increase in the shower size. In the past, attempts have been made to improve the angular resolution for small size showers, by artificially increasing the detected particle density. This is normally done by covering the scintillator detectors with a thin lead sheet, for the conversion of the low energy γ-rays in the EAS that are far more numerous, into electron–positron pairs [13].

An ideal approach for improving the angular resolution of an EAS array would be to deploy a carpet of detectors to ensure the detection of a large fraction of the shower particles in the EAS. This is also important to achieve a larger triggering efficiency for lower energy showers. The MILAGRO and the ARGO-YBJ experiments are two of the examples of this approach. The MILAGRO [14] experiment achieved full particle detection efficiency by instrumenting a 8 m deep water pond of 80×60 m^2 area, to detect Čerenkov emission produced by the shower particles inside the water pool, by the photomultipliers immersed in it. The ARGO-YBJ collaboration [15] employs resistive plate chambers to detect and time the shower particles. They have installed a carpet of resistive plate chambers, covering an area of 74×78 m^2, which is surrounded by 50% coverage over an area of 100×100 m^2. However, the total carpet area in both of these experiments is $\lesssim$6000 m^2, thereby maximizing the sensitivity of these experiments to energies below 5 TeV.

An alternative approach for improving the angular resolution of an EAS array is to decrease the inter-detector separation of the scintillator detectors. This approach provides an excellent compromise between a smaller area carpet array and a very large area sparsely instrumented array. However, the practical constraints limit the number of detectors employed in an EAS array, thereby providing only a sampling of the particle density $\rho_e(r)$ at a limited number of points. In the recent times, for example, in the Tibet ASγ [16], the CASA [17], the EAS-TOP [18], the KASCADE [19] and the GAMMA [20] arrays, the area covered by the detectors is $\lesssim$1% of the physical area over which the array is spread out. The physical area covered by the detectors in a given array, which is determined by the density of the detectors, is a key factor. This factor contributes significantly to the accuracy of the measurement of the parameters, such as the shower size 'N_e' and consequently the primary energy, as well as the arrival direction. These parameters are important in the studies in the γ-ray astronomy, at multi-TeV energies. With these definitive considerations in mind, the GRAPES-3 air shower array [21] has been designed to have one of the most compact configuration of the conventional type of EAS arrays, with a separation of only 8 m between the adjacent detectors. The GRAPES-3 detectors are arranged in a symmetric hexagonal geometry, resulting in a detector coverage of ~2% of the total area of the array.

In 1957, Clark had proposed, the use of the decrease in the isotropic flux of the cosmic ray showers, caused by the shadows of the

Moon and the Sun, for the estimation of the angular resolution of an EAS array [22]. In the past, different groups have utilized this technique of the reduction in the cosmic ray flux, due to the shadow of the Moon or the Sun, to measure not only the angular resolution, but also to obtain the absolute pointing accuracy of their EAS arrays. However, this technique works well only for those arrays that possess an angular resolution comparable to the apparent angular size (~0.5°) of these two objects in the solar system. However, the presence of the magnetic field on the surface of the Sun results in some deflection of the charged cosmic rays leading to a distortion and displacement of its shadow. The CASA [17] and HEGRA [23] collaborations had reported ~6σ deficit due to the shadow of the Moon.

The measurement of the shadow of the Moon by the Tibet ASγ experiment yielded an angular resolution of 0.5° at 10 TeV. This experiment also reported the displacement of the cosmic ray shadow of the Sun, by 0.9°W and 0.4°S relative to its optical position [24]. However, at lower energies even the magnetic field of the Earth would deflect the primary cosmic ray particles, resulting in a measurable displacement of the Moon shadow relative to its optical position. The Tibet ASγ collaboration reported a shift of 0.23°W in the shadow of the Moon, relative to its actual position. This shift was attributed to the deflection of the positively charged cosmic rays in the geomagnetic field [24].

A marginal detection of the Moon shadow in the muon flux underground was reported by the BUST group [25]. A 6.5σ deficit due to the Moon shadow in the muon flux, was detected by the MACRO collaboration [26]. The L3 collaboration had also studied the shadow of the Moon on the flux of high energy muons. A displacement of 0.8° in the Moon shadow was measured for the muons in the energy range 65–100 GeV [27,28]. Similarly the ARGO-YBJ collaboration have also reported, a displacement of 0.7°W and 0.5°N of the Moon shadow in the cosmic ray flux detected by them [29].

The present work describes the results obtained on the angular resolution and the absolute pointing accuracy of the GRAPES-3 array using the data collected over the period of 4 years from 2000 to 2003. The relevant details of the experimental system are summarized in Section 2 and the issues pertaining to the angular resolution are presented in Section 3. An extensive study of the angular resolution was carried out by using three different techniques. Two of these include, the even–odd and the left–right methods that are described in Sections 4 and 5, respectively. In the third method we have used these observations to detect the shadow of the Moon at a level of ~5σ and that of the Sun at a lower level of significance that are described in Section 6. All three techniques have yielded nearly identical results on the energy dependent angular resolution. The angular resolution of the GRAPES-3 array is found to be 1.4° at 10 TeV which improves to 0.7° at 30 TeV. These results are discussed in Section 7 and a summary is presented in the final section.

2. Experimental system

The experimental system of the GRAPES-3 (**G**amma **R**ay **A**stronomy at **P**eV **E**nergy**S** Phase-**3**) experiment consists of a densely packed array of scintillator detectors and a large area tracking muon detector as shown in Fig. 1. The EAS array consists of 257 plastic scintillator detectors, each of 1 m^2 in area. These detectors are deployed with an inter-detector separation of only 8 m. The array is being operated at Ooty in south India (11.4°N, 76.7°E, 2200 m altitude) [21].

In order to achieve the lowest possible energy threshold, a simple 3-line coincidence of detectors has been used to generate the Level-0 trigger, which acts as the fast GATE and START for the ana-
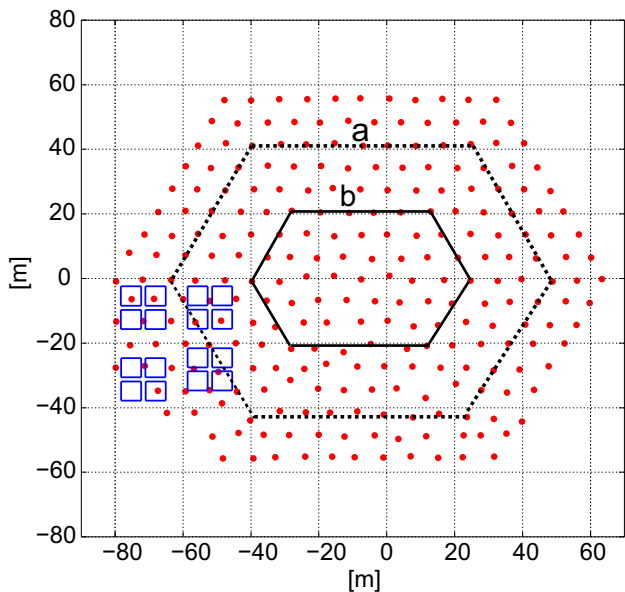
Fig. 1. The GRAPES-3 experimental system with 257 scintillator detectors (•) and 16 muon detector modules (□). The distances along the X- and Y-axes are in meters.

Fig. 2. Mean number of detectors triggered as a function of the calculated shower size, N_e.

log to digital and time to digital converters (ADCs and TDCs), respectively. As expected, this trigger selects a large number of very small and local showers and also larger showers whose cores land very far from the physical area of the array. Therefore, it is also required that at least 10 out of the inner 127 detectors should have triggered their discriminators within 1 μs of the Level-0 trigger. This Level-1 trigger with an observed EAS rate of 13 Hz is used to record the charge (ADC) and the arrival time (TDC) of the pulses from each detector. The pulse charge is later converted into the equivalent number of minimum-ionizing particles (MIPS) using the most probable charge for a single MIP measured using the trigger from a small area (20×20 cm^2) scintillation counter telescope [21].

Fig. 1 also shows 16 squares in the lower left side. Each of these squares represents a 4-layer muon tracking detector with an energy threshold of 1 GeV for the vertical muons. Each layer consists of 58 proportional counters, each 6 m long with 10×10 cm^2 cross-sectional area. The 560 m^2 GRAPES-3 muon detector consists of four super-modules, each in turn having four modules. The details of the muon detectors and their performance in relation to these physics objectives have been described in detail elsewhere [30].

3. GRAPES-3 angular resolution

A total of 1.4×10^9 showers have been collected over a total live-time of 9.4×10^7 s, spread over a 4-year period, from 2000 to 2003. For each EAS, the core location, the shower age 's' representing the steepness of the Nishimura–Kamata–Greisen (NKG) lateral distribution function and the shower size N_e have been determined [31]. This was done by using the observed particle densities, following the minimization procedure described below. For each shower, the zenith (θ) and the azimuthal (ϕ) angles have been calculated using the time information from the TDCs, also described below.

Although the number of detectors triggered by an EAS is a quantity that is experimentally well-defined, but it is not very useful when comparing the results from different experiments. For this reason we have studied the relationship between the shower size N_e and the number of detectors triggered by it. In Fig. 2, we display the mean number of detectors triggered as a function of the
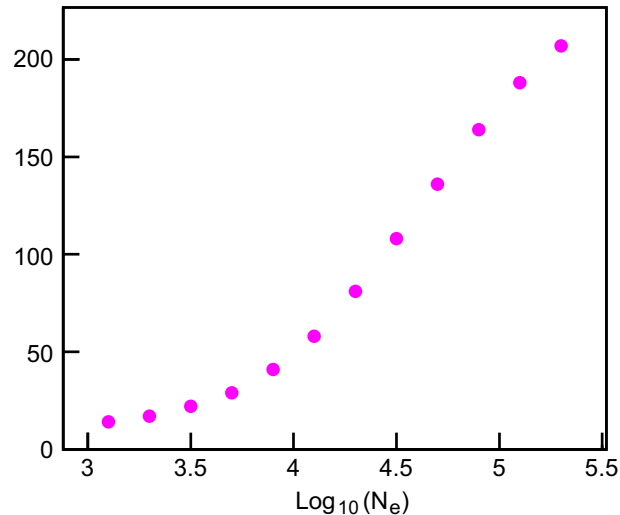
shower size, N_e. Clearly the number of triggered detectors is a less sensitive function of shower size for $N_e \leqslant 10^4$, and thereafter the increase is more rapid. The reason for this behavior is that for low shower sizes, the lateral extent of the showers is relatively small and therefore the number of detectors triggered increases rather slowly with N_e. We have estimated the uncertainty in the shower size determination due to the reconstruction errors to be ~10%. However, the errors due to the uncertainty in the hadronic interaction models are expected to be significantly larger. The error in the shower core location has been found to be ~1 m [32].

The initial values of the parameters for the shower fit were derived as described below. The timing information from the triggered detectors was used to determine the initial arrival direction (θ, ϕ) using the least square fit method assuming a plane shower front. A crude estimate of the shower size N_e was obtained from the total number of detected particles n_d in all detectors by,

$$N_e = 102 \times n_d^{0.97} \tag{1}$$

This relationship was derived from the Monte Carlo simulations of the array response using the CORSIKA code. The initial core location vector $\mathbf{R}_{core}$ was estimated from the weighted mean of the location vectors $\mathbf{r}_i$ of the top seven detectors that had recorded the highest particle densities n_i,

$$\mathbf{R}_{core} = \frac{\sum_{top_7} n_i \mathbf{r}_i}{\sum_{top_7} n_i} \tag{2}$$

It was assumed that the initial shower age $s = 1$. Next, the NKG function was used to fit the observed density in the detectors having ADC counts greater than equivalent of 0.5 particles, and the initial values of the shower direction, size, core location, age as described above. The minimization of the NKG function was carried out iteratively, by using the maximum likelihood algorithm MINUIT [33], to obtain more accurate values of various shower parameters, namely, the core location, size and age, etc. Now, by using the distance of each detector from the shower core, correction was applied at the rate of 215 ps m^{-1} to the recorded arrival time at each triggered detector, for the cone-shaped shower front as explained subsequently. This value of the correction was obtained from the shower data. This correction effectively transforms the shape of the shower front from cone into a plane. The arrival times were then fitted to a plane-shape using the least square method to obtain the final values of the arrival direction, namely, θ and ϕ.

As mentioned in the Section 1, one of the most critical parameter in the search for the point sources of cosmic γ-rays, using a particle detector array is its angular resolution. An improvement in the angular resolution allows the rejection of a larger fraction of the background EAS, initiated by the charged cosmic rays. This in turn would increase the signal to background ratio and may enable the discovery of the new cosmic γ-ray sources.

An improvement in the angular resolution in turn requires an accurate determination of the relative arrival time of the shower front at various detectors and a precise knowledge of the shape of the shower front. It may be noted that the assumption of a plane shower front is not adequate even for relatively small shower sizes. This is primarily because the particles spread out to beyond ∼50 m from the shower core. At distances ∼50 m from the core, the shower particles are delayed relative to the core because of; (i) multiple Coulomb scattering resulting in a lateral spread and consequently an added path length, (ii) transverse momenta imparted during secondary particle production also results in movement at an angle relative to the shower axis, leading to additional pathlengths. It has been experimentally shown, that a cone-shaped shower front provides an excellent description of the EAS front [24,34].

Since the detectors in the EAS array are distributed over a large area and exposed to the outside weather, the timing accuracy is affected by the temperature dependence of the response of various components of the scintillation detector system. Observations have shown that the temperature coefficient for the scintillator, the photomultiplier, the signal cables, and the electronic modules (amplifiers, discriminators and the TDCs) are significantly different from each other and undergo measurable variations.

The observed arrival time of the shower front at a detector has two components, namely t_i^s, which depends on the arrival direction (θ and ϕ) of the EAS and t_i^d, which is the transit time from the scintillator to the TDC, which includes the time response of the scintillator, the photomultiplier, the signal cables and the electronics, etc. Therefore, the time difference $t_{i,j}$ between two detectors i and j for an EAS may be written as,

$$t_{i,j} = \left(t_i^s - t_j^s \right) + \left(t_i^d - t_j^d \right)$$

In a perfectly stable system, the second component should largely remain unchanged with time which can, in principle, be determined from the EAS incident vertically. However, in practice, the second component varies with time, for example, with the ambient temperature as mentioned above, or due to the changes in; (a) the rise and the transit times in the photomultiplier, (b) the transit time in the cable from the detector in the field to the signal processing electronics in the control room, and (c) the effect of the temperature coefficient of various electronic modules such as the amplifiers, discriminators and TDCs, etc. on their propagation delay. It is easy to observe, the temperature dependence by plotting the residual time between the observed and the expected time, obtained from the arrival direction (θ and ϕ) of the EAS, from a fit of the relative arrival times, to a cone-shaped shower front through the χ^2 minimization technique.

In Fig. 3, the variation of the residual time, for three GRAPES-3 detectors, numbered 1, 3, and 5 are shown for a period of 7 days from 12 to 19 February 2001. These three detectors are located within 8 m from each other and have been selected to study the temperature dependent effects. Clearly the residual time is inversely correlated with the temperature, reaching its maximum value during the early morning hours. We understand that this effect is primarily caused by the change in the length of the signal cable from the detector to the control room, due to the change in temperature. Due to different levels of exposure of the signal cables to the sunlight, the residual time for different detectors
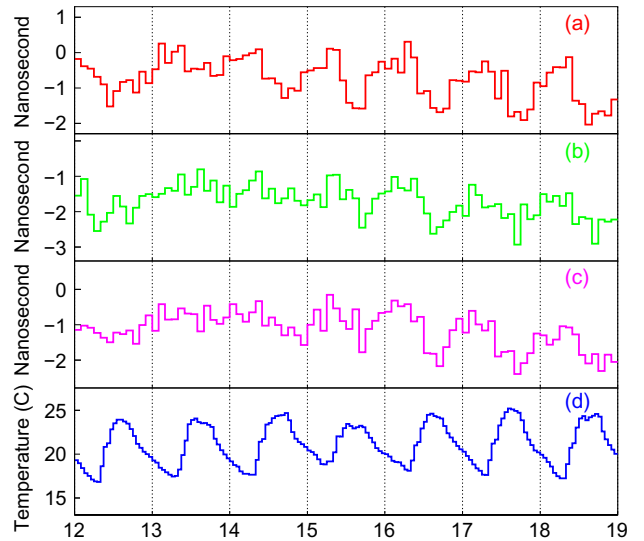

Fig. 3. Variation of the residual time for detectors 1, 3 and 5, labeled (a), (b), (c), respectively, obtained from a fit of the observed times to a cone-shaped shower front, for a period of 7 days. The minimum of the residual time occurs in the afternoon when the temperature is maximum.

are slightly different, varying within a range of ∼2 ns. Since the magnitude of this variation is relatively small and changes nearly simultaneously for all detectors, it gets nearly eliminated when calculating the relative arrival time of shower particles in the EAS for direction reconstruction. At present, attempts are being made to determine the transit time in our detector system over a period as short as an hour, for making the necessary corrections for the observed temperature dependence. However, no correction was made in the present analysis of the data discussed here. The accuracy of the angular resolution of the array discussed below is only marginally affected by the temperature dependent systematics discussed above.

4. The even–odd method

A method extensively used for estimating the angular resolution for a specific EAS array relies on the Monte Carlo simulations of the showers in the atmosphere and the response of the array to those simulated showers. This method suffers from the limitation, due to the inadequacies in the Monte Carlo simulations caused by the approximations used to reduce the computation time.

The EAS detectors in the GRAPES-3 array are sequentially numbered from the centre outwards, with the detector number increasing clockwise over each successive hexagonal ring. Therefore, it was decided to divide the array into two sub-arrays, namely, the first with the even-numbered and the second with the odd-numbered detectors. Next, a comparison of the arrival directions determined independently with the two sub-arrays, labeled 'even' and 'odd', respectively, is carried out. Since these two sub-arrays have a very substantial spatial overlap, they provide similar estimate of the EAS direction and also an important insight into the angular determination capability of the experiment [35]. An important limitation of this approach arises from the systematic errors that are common to both of the sub-arrays and therefore can not be measured. For example, there can be large systematic errors in the angles determined for a major fraction of the showers that have their axes striking the periphery of the GRAPES-3 array. But, due to the spatial overlap of the 'even' and 'odd' sub-arrays, the direction determined by them would contain the same systematic error. Therefore, the angle between these two directions would be free from this systematic error.
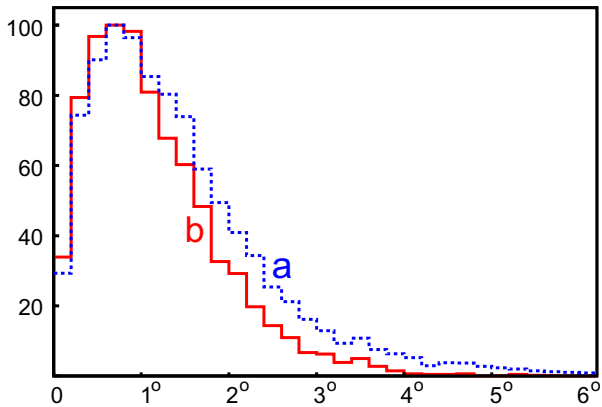
Fig. 4. Distribution of the angle between shower directions determined from 'even' and 'odd' sub-arrays, for $\geqslant 100$ detectors triggered, (a) all events, (b) shower core within dashed hexagon labeled 'a' in Fig. 1. Peak value on y-axis normalized to 100 for easy comparison.
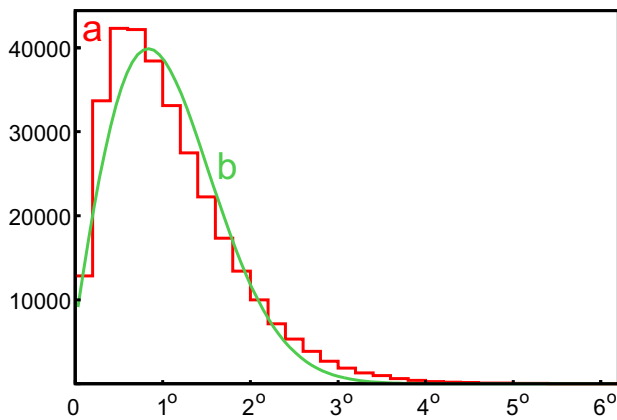

Fig. 6. Variation of the median angle α_M as a function of the number of detectors triggered.

Fig. 5. Distribution of the angle between shower directions determined from, (a) even and odd sub-arrays for $\geqslant 100$ detectors triggered, (b) 2-D Gaussian fit yields a $\sigma = 0.94°$.

Since the shielding coverage of the muon detector extends only up to 45°, the showers for further analysis have been selected up to a maximum zenith angle of 40°. The distribution of the angle between the EAS arrival directions, determined by the 'even' and 'odd' numbered sub-arrays are shown in Fig. 4, by the dashed histogram labeled 'a'. The selected showers were required to trigger at least 100 detectors, which corresponds to a shower size N_e of $10^{4.5}$ as shown earlier in Fig. 2. Thus on an average each sub-array would have information from $\geqslant 50$ detectors. A further cut was imposed on the location of the shower core to lie within the hexagon labeled 'a', as shown in Fig. 1. The resulting angular distribution for the even and odd sub-arrays is shown in Fig. 4, by the histogram labeled 'b'. The peak value of the two distributions in Fig. 4 has been normalized to 100 for an easy comparison. This figure clearly shows that the error in the determination of the direction improves when a cut on the core location is imposed. The error in arrival direction for the shower size considered here, is relatively small. To estimate the angular resolution, we have fitted the distribution labeled 'b' in Fig. 4 to a 2-dimensional Gaussian [36]. The even–odd angular distribution with the core cut is shown in Fig. 5 by the histogram labeled 'a', and the 2-D Gaussian fit with the label 'b'. A value of the $\sigma = 0.94°$ is obtained for the standard deviation from this 2-D Gaussian fit.

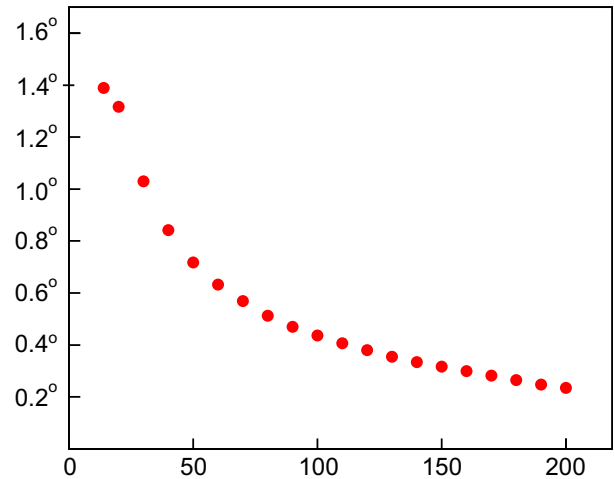Since the data from these two sub-arrays are independent of each other, the actual error in the determination of the angle is smaller by a factor of $\frac{1}{\sqrt{2}}$, than the value quoted above. Since, only half of the total number of detectors triggered, are used in each of the two sub-arrays, the angular resolution for the full array would be smaller by a further factor of $\frac{1}{\sqrt{2}}$. Therefore, the true angular resolution would be $0.94°/2 = 0.47°$, for showers triggering $\geqslant 100$ detectors, which corresponds to a shower size of $\geqslant 10^{4.5}$ as is shown earlier in Fig. 2. However, it needs to be emphasized here, that the even–odd method provides an estimate of only the statistical error in the angle determination, and it does not permit the evaluation of the systematic error in the measurement of the arrival direction. Therefore, the value of 0.5° represents the best possible angular resolution attainable for the GRAPES-3 array, for a shower size N_e of $\geqslant 10^{4.5}$.

In the earlier discussion, we had used only those showers that had triggered $\geqslant 100$ detectors. But the angular resolution of an EAS array is a function of the number of detectors triggered. Therefore, next we examine the distribution of the angle α_{eo} determined from even and odd sub-arrays as a function of the number of detectors triggered and then calculate the median angle α_M of the α_{eo} distribution. In Fig. 6, the median angle α_M, which is also an alternative measure of the angular resolution of our array, is shown as a function of the number of detectors triggered. The magnitude of the median angle α_M initially decreases rapidly with increasing number of triggered detectors up to $\sim$50 detectors, indicating rapid improvement in the angular resolution. However, thereafter the improvement is relatively slower.

As described in the beginning of Section 3, the size of each shower is determined by fitting the NKG function [31] to the lateral distribution of the observed shower densities. Thereafter, the showers in a narrow size range of $10^x - 10^{x+0.2}$ are selected, where $3.2 \leqslant x \leqslant 5.4$, and the distribution of the number of detectors triggered is obtained. In Fig. 7, the distribution of the number of detector triggered for a shower size range of $10^{4.4} \leqslant N_e \leqslant 10^{4.6}$ is shown. A Gaussian fit to this distribution yields a mean of 111 with a rather narrow rms spread of 15, implying a fractional width of only 13%. Therefore, the number of detectors triggered appears to be a fairly good measure of the shower size, provided a sufficiently narrow range of the shower size is selected.

The dependence of the angular resolution on the zenith angle has been studied by dividing the zenith angle range from 0 to 40° into five bins, namely, 0–13°, 13–19°, 19–25°, 25–32°, and 32–40°. This particular choice of angular segmentation was implemented to ensure that the number of showers present in each of the five bins are rather similar to each other. The angular resolu-
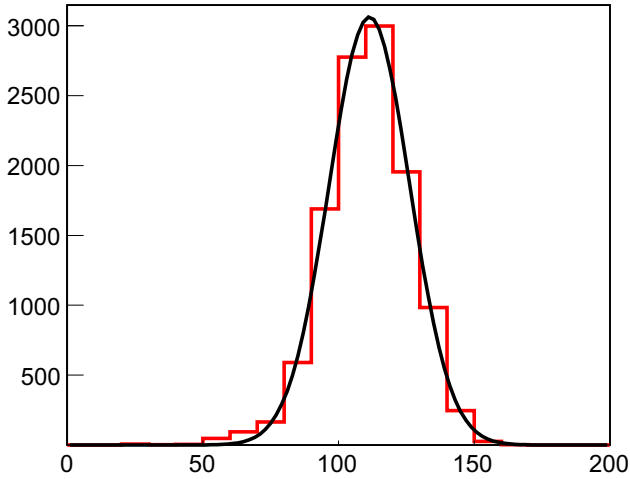
Fig. 7. The distribution of the number of detectors triggered for a narrow size range of $10^{4.4} \leqslant N_e \leqslant 10^{4.6}$. Gaussian fit yields a mean of 111 and $\sigma = 13\%$.
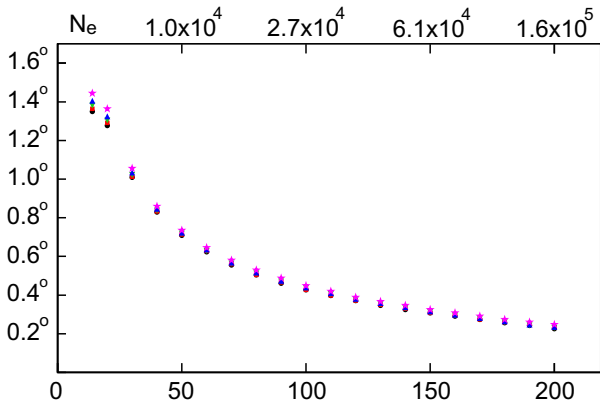

Fig. 8. Variation of angular resolution with number of triggered detectors for five zenith angle bins, (a) 0–13°, circle ●, (b) 13–19°, square ■, (c) 19–25°, inverted triangle ▼, (d) 25–32°, triangle ▲, (e) 32–40°, star ★, respectively. Shower size N_e is shown at top along secondary x-axis.

tion as a function of the number of detectors triggered for, (a) 0–13° by circle ●, (b) 13–19° by square ■, (c) 19–25°, by inverted triangle ▼, (d) 25–32°, triangle ▲, and (e) 32–40°, star ★ are shown in Fig. 8. The corresponding shower size N_e is displayed at the top along the secondary x-axis in Fig. 8 for an easy comparison, at the location of the markers. The angular resolution shows a rather weak dependence on the zenith angle for the range of 0–40° studied here. The magnitude of the angular resolution increases gradually with the increasing zenith angle as seen from Fig. 8. The increase in the angular resolution relative to the first bin shown as ● is; ~0.8% for the second bin ■, ~1.6% for the third bin (▼), ~2.9% for the fourth bin (▲), and ~5.6% for the fifth bin (★), respectively. In the subsequent discussion we examine the data by two other alternative methods to evaluate the actual angular resolution achieved.

5. The left–right method

In the beginning of Section 3, we had mentioned that a cone-shaped shower front has been used for determining the arrival direction of an EAS. Here, we present the results of a study that demonstrates the presence of the curvature in the shower front. A considerable improvement is seen in the angular resolution
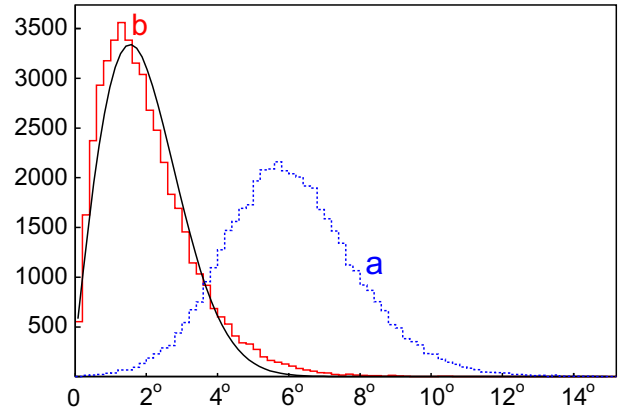

Fig. 9. Distribution of angle α_p between EAS directions determined from (a) left- and the right-half arrays for $10^{4.4} \leqslant N_e \leqslant 10^{4.6}$, (b) 2-D Gaussian fit with a $\sigma = 1.64°$.

when a cone-shape is used to describe the curvature of the shower front. The curvature of the shower front is readily studied by dividing the array into two independent halves, namely, the left- and the right-half arrays. For this purpose the following procedure is adopted. First, the location of the shower core is determined and then the line joining the shower core with the centre of the array is used to divide the array into the left- and the right-half arrays. Although this array division is implemented on an event-to-event basis, yet this procedure ensures that the number of detectors triggered in each of the two half-arrays are approximately equal.

In the even–odd case, the density of the detectors is reduced by a factor of 2, while the area of the each sub-array remains nearly the same as the area 'A' of the full array. However, in the left–right case the density of the detectors remains unchanged, but the area of each half-array gets reduced to $\frac{A}{2}$. Therefore, we expect the ratio of the areas in the two cases to be 2. Since the angular resolution is inversely proportional to the linear extent of the array, we expect the angular resolution to worsen by a factor of $\frac{1}{\sqrt{2}}$ in the left–right case, as compared to the even–odd case. Therefore, correction by an additional factor of $\frac{1}{\sqrt{2}}$ is required when comparing the results from the above methods.

A stringent cut is imposed, on the location of the shower core to lie within the hexagon labeled 'b' in Fig. 1. This is done to ensure the selection of the showers landing in the central region of the array. The direction of a given shower is determined independently, by each half-array (θ_L, ϕ_L and θ_R, ϕ_R), by assuming a plane shower front. Next, the angle α_p between these two shower directions given by θ_L, ϕ_L and θ_R, ϕ_R is calculated. In Fig. 9, the distribution of α_p is shown labeled 'a', for a shower size range of $10^{4.4} \leqslant N_e \leqslant 10^{4.6}$. Clearly the large width of α_p distribution with a mean value in excess of 6° indicates that the plane-shape does not provide an appropriate description of the shower front. Several studies done in the past had demonstrated that the shower front is adequately represented by a cone-shape [37–40].

We have also found that the GRAPES-3 data can be very well fitted to a cone-shaped EAS front. The cone-shaped front also results in a large reduction in the angle α_c between the left and the right half-arrays. The best fit yielded a value of 215 ps m^{-1} for the slope of the cone, relative to the plane perpendicular to the shower axis. The distribution of α_c is shown labeled 'b' in Fig. 9. The large improvement in the angular resolution due to the use of the cone-shaped front may be judged from the difference in the width of the distributions of α_p and α_c. Also shown on the same plot is a 2-D Gaussian fit to the α_c distribution. A value of $\sigma = 1.64°$ was obtained for the standard deviation from this fit. However, the value of 1.64° has to be corrected for the systematically smaller area
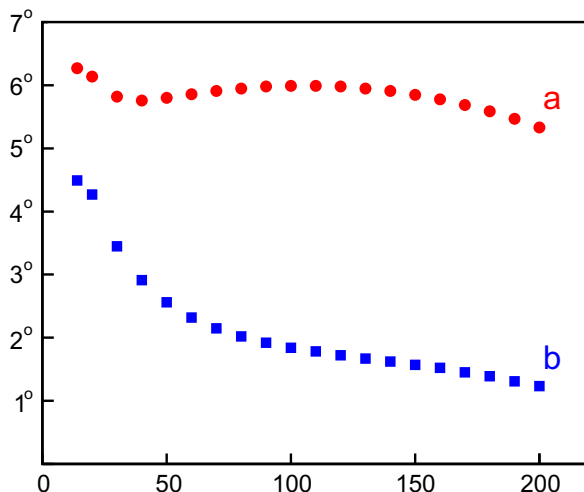
Fig. 10. Variation of the median angle, (a) α_{mp} for plane fit shown by filled circles •, (b) α_{mc} for cone fit shown by filled squares ■, as a function of number of detectors triggered.

Fig. 11. Concentric circles drawn around Moon or Sun directions of equal solid angle. First ring has a diameter of 1.26°.

(A_L, A_R) of the left–right arrays, as compared to the area (A_E, A_O) of the even–odd arrays as explained above. But instead of applying the correction factor due to area calculated above, we have investigated this problem by utilizing the experimental data.

We have classified the showers according to the number of detectors triggered. The values of the areas A_E, A_O, A_L and A_R are calculated using the area covered by the triggered detectors for each shower. The distribution of the ratio of A_E and A_O is extremely narrow and centred at 1. Therefore, we decided to use $A_{EO} = \frac{A_E + A_O}{2}$ as the area for the even–odd case, for a given number of detectors triggered. Nearly identical results have also been obtained in the left–right cases as well. Therefore, we have used $A_{LR} = \frac{A_L + A_R}{2}$ as the area for the left–right case. The values of A_{EO} and A_{LR} are found to be different and both increase with increasing number of detectors triggered. However, the ratio $R = \frac{A_{EO}}{A_{LR}}$ is found to be constant and independent of the number of detectors triggered. The value of R is found to be 2.002, almost same as the expected value of 2 as discussed above. When this area dependent correction is applied, we get an effective angular resolution of 1.15° which is only marginally larger than the value of 0.94° obtained by the even–odd method as shown in Fig. 5. This is not surprising, because as explained earlier in Section 4, the even–odd method represents the best possible angular resolution attainable by a given array.

As described in Section 4, the angular resolution of an EAS array is a function of the number of detectors triggered. In the earlier discussion, we had used the EAS in the shower size range of $10^{4.4} \leqslant N_e \leqslant 10^{4.6}$ that triggered a mean of 111 detectors. Next we examined, for a given number of triggered detectors the distribution of the angle α_p determined from the left- and right-half arrays using a plane EAS front. We then calculated the median angle α_{mp} from the α_p distribution. In Fig. 10, the median angle α_{mp} is shown as filled circles, as a function of number of detectors triggered. The magnitude of α_{mp} shows a very small change with increasing number of triggered detectors, right up to 200 detectors. Using an identical procedure the value of the median angle α_{mc} is calculated for the cone-shaped EAS front. In Fig. 10, the median angle α_{mc} is displayed as filled squares, as a function of number of detectors triggered. The magnitude of α_{mp} initially decreases rapidly with increasing number of triggered detectors up to ~50 detectors, indicating a rapidly improving angular resolution, however, thereafter the improvement becomes relatively slower. A study of the dependence of the angular resolution on the zenith angle was carried out using the method described in Section 4. The
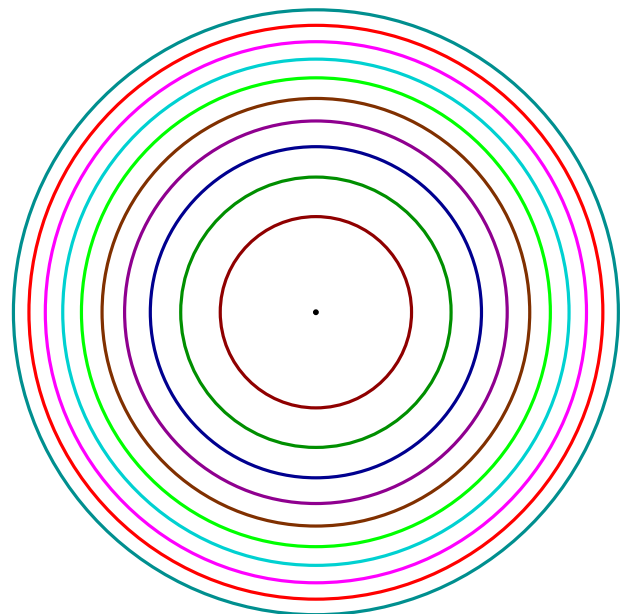
results of this study also showed a weak dependence of the angular resolution on the zenith angle, similar to the one shown in Fig. 8.

6. Shadows of Moon and Sun

It is well-known that the observations of the shadow of the Moon or the Sun cast on the flux of the cosmic rays observed at the Earth provides an ideal method to determine the angular resolution of an EAS array. It allows both, the statistical error in the angle determination, as well as the systematic error in 'pointing' towards a given direction to be measured. The shadows due to the Moon and the Sun on the cosmic ray flux has been observed for various primary energies by several groups. The shadow of the Moon in the flux of the secondary muons has been observed; in a deep mine by the Soudan group [41], in the underground MACRO detector [26] and inside the L3 detector at CERN [42]. The MILAGRO collaboration have also studied the shadow of Moon at energies ~1 TeV using a water pond as an EAS array [43].

The following procedure has been adopted for the analysis of the GRAPES-3 shadow data; divide the field of view of radius 4° around the centre of the Moon or the Sun, into 40 concentric circles of equal solid angle area. The inner 10 rings are shown schematically in Fig. 11. Next, the number of showers incident along directions lying within each concentric bin are counted. The inner most bin (disk) has a diameter of 1.26°, which is ~2.5 times the angular diameter of the Moon. The solid angle of each bin is 3.8×10^{-4} sr, which is ~6.4 times the solid angle projected by the Moon or the Sun. This choice of binning was dictated by the anticipated angular resolution of the GRAPES-3 array which was ~1° and a solid angle segmentation smaller than this value would have resulted in excessive amount of over-sampling. For a comparison, similar concentric circles were drawn centred on two different directions, on either side of the Moon (or the Sun) that are offset by 8° in the azimuthal angle, but at the same zenith angle. This selection of the background region ensures that the shower attenuation in both the Moon/Sun and background regions is identical and concurrent. This analysis showed a uniform distribution indicating the absence of any shadowing effects along these two directions away from the Moon and the Sun. However, this data was not used for any further studies.
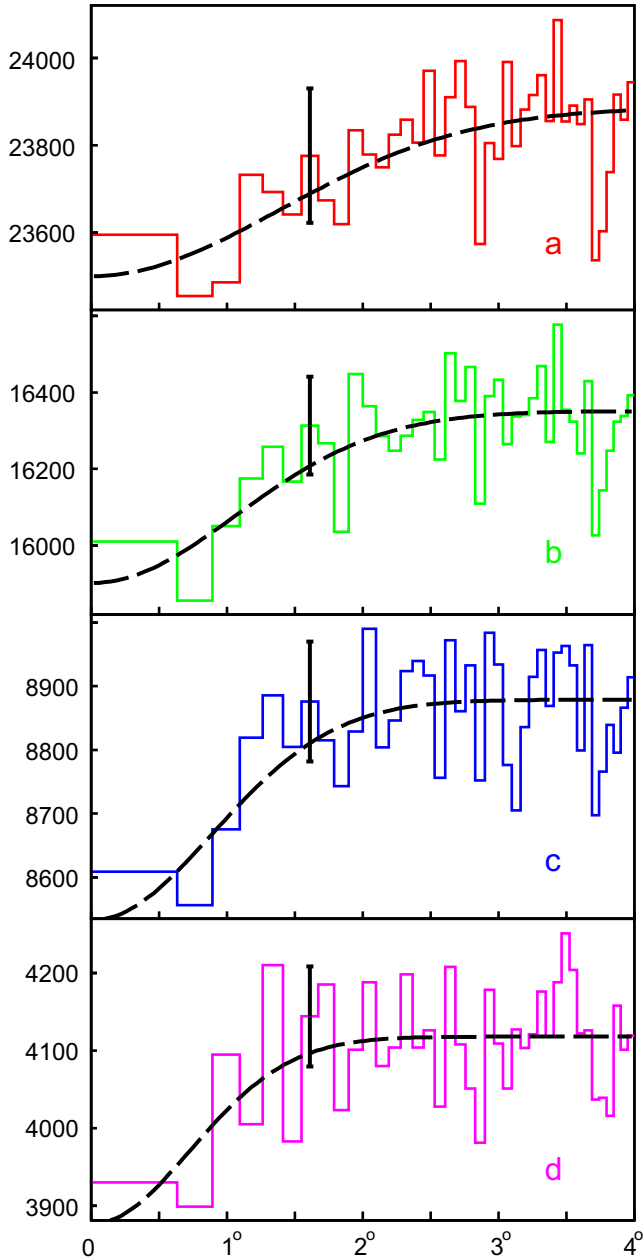
Fig. 12. Number of EAS in 3.8×10^{-4} sr concentric bins around Moon for shower size N_e, (a) $\geqslant 10^{3.2}$, angular resolution $\sigma = 1.39° \pm 0.17°$, (b) $\geqslant 10^{3.5}$, $\sigma = 1.07° \pm 0.13°$, (c) $\geqslant 10^{3.75}$, $\sigma = 0.89° \pm 0.10°$, (d) $\geqslant 10^{4.0}$, $\sigma = 0.73° \pm 0.09°$. Dashed lines represent 2-D Gaussian fits.

The data collected over a 4-year period from 2000 to 2003 are used in the study described below. The histogram in Fig. 12a shows, the variation in the number of showers of size $N_e \geqslant 10^{3.2}$, for the incident EAS directions in the annular regions of the concentric rings of equal solid angle as displayed in Fig. 11. The total exposure time for the Moon is 2.1×10^7 s. The first bin of the histogram in Fig. 12a is centred on the Moon. A reduction in the flux of showers in the direction of the Moon is clearly seen. The dashed line in Fig. 12a is a 2-D Gaussian fit to the deficit in the data and the bar represents the $\pm 1\sigma$ error. The deficit in counts described by the 2-D Gaussian is given by the following equation:

$$N(\theta) = N_o \left(1 - \frac{\theta_M^2}{2\sigma^2} \exp\left[-\frac{\theta^2}{2\sigma^2} \right] \right) \qquad (3)$$

where θ_M is the radius of the Moon or the Sun, N_o is a constant that represents the unshadowed background shower rate and σ is the standard deviation of the 2-D Gaussian fit and represents the angular resolution of the array. The values of N_o and σ are obtained from the 2-D Gaussian fit. Based on this fit, the angular resolution of the GRAPES-3 array was estimated to be $\sigma = (1.39° \pm 0.17°)$, $N_o = 23886$ for the showers of size larger than $10^{3.2}$ particles. For calculating the deficit in the number of showers, the optimum angular radius for a Gaussian distribution is given by $1.58 \times \sigma = 1.58 \times 1.39° = 2.2°$, which corresponds to the 12 innermost solid angle bins. The deficit N_d in the number of showers around the direction of the Moon, relative to the mean shower rate of N_o per bin may be calculated as follows. Following the procedure described above we find the total number of showers in the innermost 12 bins, $N_{moon} = \sum_{i=1}^{12} N_i = 284,029$ as against an expected mean $N_{expt} = 12 \times N_o = 12 \times 23,886 = 286,632$. The observed deficit $N_d = N_{expt} - N_{moon} = 286,632 - 284,029 = 2603$. Therefore, the significance of this deficit is, $N_d/\sqrt{N_{expt}} = 2603/\sqrt{286,632} = \sim 5\sigma$.

The histogram in Fig. 12b represents the data for the shower size $N_e \geqslant 10^{3.5}$. Here also a clear decrease in the shower rate is visible. The 2-D Gaussian fit to this data yields an angular resolution $\sigma = (1.07° \pm 0.13°)$ for the shower size threshold listed above. Similarly the data for the shower size $N_e \geqslant 10^{3.75}$ is shown in Fig. 12c and the 2-D Gaussian fit to the data yields an angular resolution $\sigma = (0.89° \pm 0.10°)$. Finally, the data for the shower size $N_e \geqslant 10^{4.0}$ are shown in Fig. 12d and the 2-D Gaussian fit yields an angular resolution $\sigma = (0.73° \pm 0.09°)$.

Since the EAS recorded by the GRAPES-3 experiment are of relatively high energy ($\geqslant 15$ TeV), the deflection in the geomagnetic field is expected to be very small. Therefore, the location of the Moon shadow may be used to obtain the absolute pointing accuracy of the GRAPES-3 array. The minima of the Moon shadow appears to lie within $\pm 0.2°$ in the right ascension and declination of the centre of the Moon. Therefore, we conclude that the absolute pointing accuracy of the GRAPES-3 array is $\sim 0.2°$.

As compared to the 1-dimensional histogram shown in Fig. 12 a 3-dimensional color coded map of the decrease in the number of showers due to the shadow of the Moon is more informative. In Fig. 13, the 3-dimensional map of the number of showers arriving from the directions around the Moon are shown. The map is centred on the Moon and covers $\pm 5°$ both in the right ascension and the declination. The magnitude of the shadow is parametrized as percentage change in the flux of isotropic cosmic rays. The shape of the shadow of the Moon on the primary cosmic ray flux is clearly visible in Fig. 13. In the earlier discussion in Section 4, we had employed a 2-D Gaussian in the study of the angular resolution of our array. Similarly in Section 6, to measure the effect of the shadows of the Moon and the Sun, we have again employed the 2-D Gaussian fit. Although there are sizable fluctuations near the outer periphery of the shadow, a sharp and reasonably symmetric shadow, centred on the direction of the Moon is clearly visible.

It may be mentioned here that the shadow of the Moon on the cosmic ray flux is a straightforward case of the physical blocking by the Moon. However, in the case of the Sun, the magnetic field of the Sun and the solar activity in its vicinity also plays an important role in causing a deflection in the path of cosmic rays, in addition to physical blocking. The structure of the magnetic field around the Sun is also very complex with frequent temporal changes. As reported by the Tibet ASγ [44] and ARGO-YBJ [45] collaborations, the shadow pattern due to the Sun evolves with time, resulting in a rather blurred image when integrated over a period of several years. We observed the shadowing effects from the direction of the Sun, although with significantly larger fluctuations. This is not unexpected, since our observations during 2000–2003 coincided with the period of maximum solar activity.
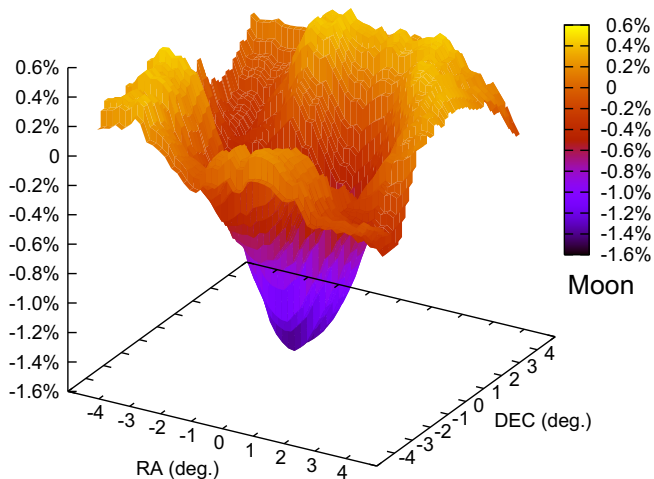
Fig. 13. A 3-D profile of the number of showers arriving from directions around the Moon. The map is centred on the Moon and covers ±5° in R.A. and declination. A clear and reasonably symmetric shadow, centred on the Moon is visible.
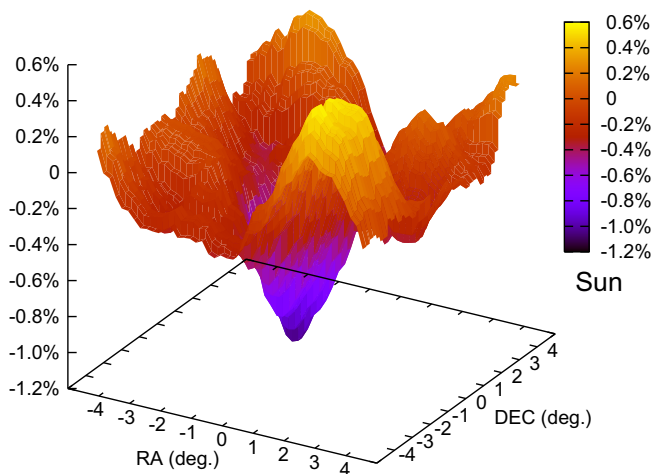

Fig. 15. The *x*-axis shows the shower size N_e and corresponding primary proton energy in TeV, is shown on the *y*-axis. Number of detectors triggered #D are shown at top along secondary *x*-axis.

interplanetary magnetic field associated with the higher solar activity due to the solar maximum, during a major part of the 4 year observation period of the GRAPES-3 data. It may also be noted that in Fig. 14, the minima of the shadow appears to be offset, by 0.4°W and 0.2°S relative to the centre of the Sun. This displacement (0.4°W, 0.2°S) of the Sun shadow relative to its optical position, is along the same direction (0.9° W, 0.4°S) as was reported by the Tibet ASγ collaboration [24]. The magnitude of the displacement observed by us is about a factor of 2 smaller as compared to Tibet ASγ. This is not unreasonable, in view of the fact that the energy threshold for the GRAPES-3 is larger than Tibet ASγ, which would result in a smaller deflection of the charged particles due to a given magnetic field in the solar vicinity. However, given the relatively large fluctuations in the shape of the shadow, the magnitude of the observed offset (0.4°W, 0.2°S) is also not inconsistent with a null value.

7. Discussion

For a direct comparison of the angular resolution of the GRAPES-3 array by the use of three different methods, we have converted the shower size N_e into the energy of the primary protons, using the CORSIKA Monte Carlo simulation program, version 6.500 with the QGSJet generator [46]. Although the primary cosmic rays contain heavier nuclei, their contribution at any given shower size N_e is relatively small for energies below 100 TeV considered here. In Fig. 15, the derived median primary proton energy is shown as a function of the observed shower size N_e. The shower size N_e is plotted on the *x*-axis and the primary energy in TeV is displayed on the *y*-axis. This plot is used to convert the shower size into the primary proton energy for further discussions. In the earlier discussion, the dependence of the angular resolution was studied, as a function of either the number of detectors triggered or the shower size N_e. However, in the following, the relation between shower size and number of detectors triggered as shown in Fig. 2, and the relation between shower size and primary energy as shown in Fig. 15 has been used for conversion into equivalent primary energy. At the top of Fig. 15, the corresponding number of detectors triggered for a given N_e are also displayed along the secondary *x*-axis for an easy comparison.

A comparison of the angular resolution of the GRAPES-3 array, as determined by the three completely independent methods

Fig. 14. A 3-D profile of the number of showers from directions around the Sun. The map is centred on Sun and covers ±5° in R.A. and declination. shadow centred on Sun is visible.

The total GRAPES-3 exposure time for the Sun is 2.2×10^7 s. Now, we display the shadow of the Sun in a 3-dimensional map of the number of showers arriving from the directions around the Sun in Fig. 14. This map is centred on the Sun and covers ±5° both in the right ascension and declination. The magnitude of the shadow is parametrized as percentage change in the flux of isotropic cosmic rays. The effect of the shadow of the Sun is visible in Fig. 14, although it appears to be a lot more fuzzy than the shadow of the Moon which was shown in Fig. 13. Although the Sun data show significantly larger fluctuations specially in the outer region of the shadow, yet a clear shadow is still discernible.

The smaller deficit with lesser significance for the shadow of the Sun with a more fuzzy shape as seen in Fig. 14 may be due to the effect of the turbulent magnetic field around the Sun. In addition, the structure of the magnetic field around the Sun is rather complex with frequently occurring time dependent changes. These changes in the solar magnetic field are expected to influence the shadow pattern, resulting in a blurred images when integrated over a long period of time. A significant contribution to the observed blurring of the shadow may also be due to the turbulent
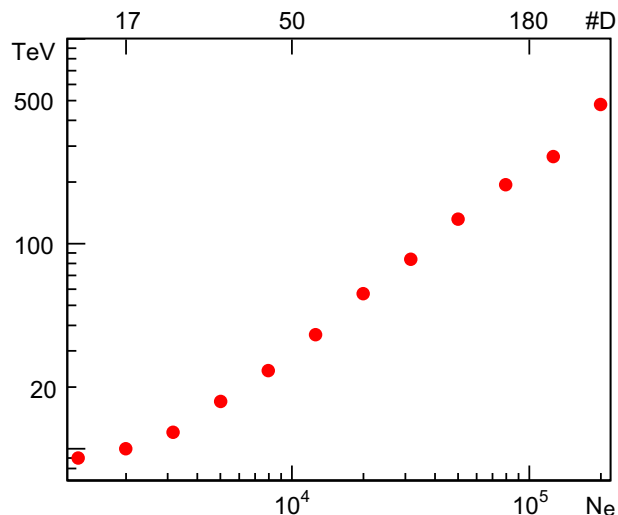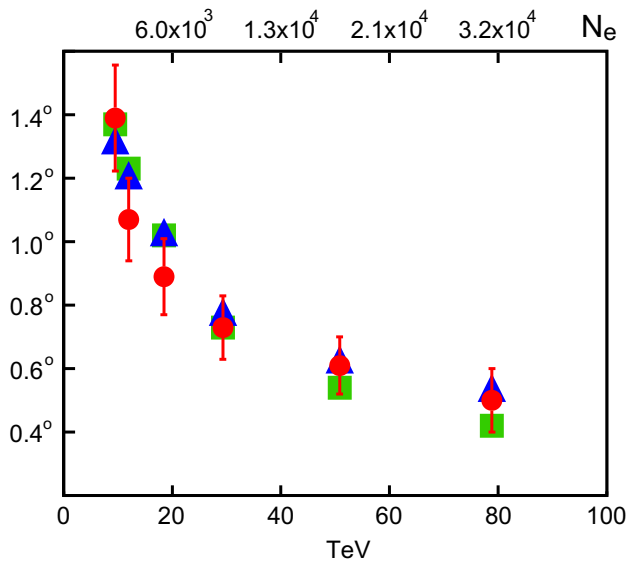
Fig. 16. Variation of angular resolution with primary energy (TeV) by three methods, (a) even–odd, filled squares (■), (b) left–right, filled triangles (▲), (c) Moon shadow, filled circles (●). Shower size N_e is shown at top along secondary x-axis.

namely; the even–odd, the left–right and the Moon shadow, as outlined in Sections 4–6, respectively, are shown in Fig. 16. For the even–odd case the angular resolution is extracted from the 2-D Gaussian fit to the angular distribution of events for a given number of detectors triggered. This value is divided by 2, as explained in Section 4, to obtain the true value of the angular resolution. The number of triggered detector is converted into shower size by using the relationship shown in Fig. 2 and then into the primary energy by using the dependence shown in Fig. 15. Also shown at the top of Fig. 16 is the corresponding shower size N_e along the secondary x-axis for an easy reference. Finally, the angular resolution of the GRAPES-3 measured by the even–odd method, as a function of the primary energy is shown by filled squares in Fig. 16. The resolution of the array improves with the increasing primary energy from 1.3° at 10 TeV to 0.4° at 80 TeV.

Using the same technique used for the even–odd case, the angular resolution as a function of primary proton energy is calculated for the left–right method. However, the value of the resolution is divided by a further factor of $\sqrt{2}$ for the reasons outlined in Section 5. The resolution of the array is 1.3° at 10 TeV, which is nearly the same as measured by the even–odd method. However, the improvement is marginally smaller at higher energies with a value of 0.5° being observed at 80 TeV. The angular resolution measured by the left–right method, as a function of the primary energy is displayed by filled triangles in Fig. 16.

The Moon shadow data also show a very similar behavior with an angular resolution of 1.4° at 10 TeV, which improves to 0.5° at 80 TeV. The resolution measured by the Moon shadow, as a function of the primary energy is shown by filled circles in Fig. 16. However, due to the limited statistics of the data on the Moon shadow, the statistical errors are not very small. It is to be noted that the Moon shadow results are consistent with those obtained from the other two methods. Clearly, the values of the angular resolution derived from the three completely independent methods are nearly identical. This fact provides the confidence in the cone-shaped shower front being an adequate description of the observed EAS in the GRAPES-3 experiment. It also implies that the determination of the angular resolution of the GRAPES-3 is reliable and largely free from systematic errors. Using the Moon shadow we estimate the absolute pointing accuracy to be ~0.2°.

8. Summary

We have analyzed the EAS data collected by the GRAPES-3 experiment over the 4-year period from 2000 to 2003. The division of the array into even and odd sub-arrays is used to estimate the shower energy dependent angular resolution of the GRAPES-3 array. An alternative method of estimating the angular resolution by using the concept of left and right half-arrays with cone-shaped shower front has yielded a value of 0.5°, which is slightly larger than the value of 0.4° obtained by the even–odd method for showers of energy ⩾80 TeV. The even–odd method provides the best estimate of the angular resolution attainable, in an array, free from systematic errors. The agreement between the angular resolution obtained from the even–odd and the left–right methods provides the evidence, that the cone-shaped shower front used in determining the shower direction is an adequate representation of the shower disk. Finally, the reduction in the isotropic flux of the cosmic rays due to the shadow of the Moon yields an angular resolution of 0.5° for showers of energy ⩾80 TeV. The absolute pointing accuracy of the GRAPES-3 arrays is ~0.2° and the small offset observed, based on the present data set, is consistent with a null value. The Sun data also yields a similar value of the angular resolution, although with significantly larger uncertainty for the reasons outlined in Section 6. We conclude that the high density of the detectors in the GRAPES-3 experiment has been instrumental in obtaining the observed angular resolution.

Acknowledgments

References

[1] R. Blandford, D. Eichler, Phys. Rep. C 154 (1987) 1.
[2] M.A. Malkov, L.O.C. Drury, Rep. Prog. Phys. 64 (2001) 429.
[3] A.R. Bell, MNRAS 353 (2004) 550.
[4] M. Ruderman, Ann. Rev. Astron. Astrophys. 10 (1972) 427.
[5] C.F. Kennel, F.V. Coroniti, Astrophys. J. 283 (1984) 694.
[6] F.V. Coroniti, Astrophys. J. 349 (1990) 538.
[7] F.C. Michel, Astrophys. J. 431 (1994) 397.
[8] A. Achterberg et al., MNRAS 328 (2001) 393.
[9] S.K. Gupta et al., Astrophys. Space Sci. 115 (1985) 163.
[10] T.C. Weekes, Phys. Rep. 160 (1988) 1.
[11] S.K. Gupta et al., J. Phys. G: Nucl. Part. Phys. 17 (1991) 1271.
[12] D.E. Alexandreas et al., Phys. Rev. D 43 (1991) 1735.
[13] S.D. Bloomer, J. Linsley, A.A. Watson, J. Phys. G: Nucl. Part. Phys. 14 (1988) 645.
[14] R. Atkins et al., Nucl. Instr. Methods A 449 (2000) 478;
    R. Atkins et al., Astrophys. J. 595 (2003) 803.
[15] C. Bassi et al., Nucl. Instr. Methods A 443 (2000) 342;
    C. Bassi et al., Astropart. Phys. 17 (2002) 151.
[16] M. Amenomori et al., Nucl. Instr. Methods A 288 (1990) 619.
[17] A. Borione et al., Nucl. Instr. Methods A 346 (1994) 329;
    A. Borione et al., Phys. Rev. D 49 (1994) 1171.
[18] M. Aglietta et al., in: Proc. 22nd Int. Cosmic Ray Conf. Dublin, vol. 2, 1991, p. 708.;
    M. Aglietta et al., Astropart. Phys. 3 (1995) 1.

[19] T. Antoni et al., Astropart. Phys. 14 (2001) 245;
     T. Antoni et al., Nucl. Instr. Methods A 513 (2003) 490.
[20] Y.A. Gallant et al., in: Proc. 29th Int. Cosmic Ray Conf. Pune, vol. 4, 2005, p. 85.
[21] S.K. Gupta et al., Nucl. Instr. Methods A 540 (2005) 311.
[22] G.W. Clark, Phys. Rev. 108 (1957) 450.
[23] M. Merck et al., Astropart. Phys. 5 (1996) 379.
[24] M. Amenomori et al., Phys. Rev. D 47 (1993) 2675;
     M. Amenomori et al., Astropart. Phys. 28 (2007) 137.
[25] Yu.M. Andreyev et al., Cosmic Res. 40 (2002) 559.
[26] M. Ambrosio et al., Astropart. Phys. 20 (2003) 145.
[27] P. Achard et al., Astropart. Phys. 23 (2005) 411.
[28] L.W. Jones, Czech. J. Phys. Suppl. A 56 (2006) 201.
[29] Y. Wang et al., Nucl. Phys. B (Proc. Suppl.) 175–176 (2008) 551.
[30] Y. Hayashi et al., Nucl. Instr. Methods A 545 (2005) 643.
[31] K. Greisen, Ann. Rev. Nucl. Sci. 10 (1960) 63.
[32] H. Tanaka et al., in: Proc. 29th Int. Cosmic Ray Conf. Pune, vol. 6, 2005, p. 209.;
     H. Tanaka et al., Nucl. Phys. B (Proc. Suppl.) 175–176 (2008) 280.
[33] F. James, MINUIT, CERN Prog. Library D506, 1998.
[34] S.Z. Chen et al., Nucl. Phys. B (Proc. Suppl.) 175–176 (2008) 435.
[35] S.C. Tonwar, in: R.J. Protheroe, S.A. Stephens (Eds.), Workshop on Techniques in
     UHE γ-ray Astronomy, Univ. of Adelaide, La Jolla, 1985, p. 40.
[36] M. Aglietta et al., Nucl. Instr. Methods A 336 (1993) 310.
[37] S. Gamp et al., Phys. Rev. D 46 (1992) 2831.
[38] R.V. Vasilev et al., Instr. Exp. Tech. 45 (2002) 631.
[39] P. Bauleo, C. Bonifazi, A. Filevich, Nucl. Instr. Methods A 516 (2004) 425.
[40] G. Marsella et al., J. Phys. Conf. Ser. 39 (2006) 475.
[41] J.H. Cobb et al., Phys. Rev. D 61 (2000) 092002.
[42] Z. Yao et al., Nucl. Phys. B Proc. Suppl. 175–176 (2008) 294.
[43] D. Berley et al., in Proc. 25th Int. Cosmic Ray Conf. Durban, vol. 5, 1997, p. 241.
[44] M. Amenomori et al., Astrophys. J. 541 (2000) 1051;
     M. Amenomori et al., Adv. Space Res. 38 (2006) 936.
[45] G.D.A. Staiti et al., Nucl. Instr. Methods A 588 (2008) 7.
[46] http://www-ik.fzk.de/corsika.